Drainage pattern as a tectonic footprint: A case study of Riedel conjugate systems in the Laguna del Maule Volcanic Complex, Southern Andean Volcanic Zone (Chile)

A. Pastor[1]

[1] Departamento de Obras Civiles y Geología, Universidad Católica de Temuco

Corresponding author: Alvar Pastor (apastor@uct.cl)

Key Points:

- Two conjugate Riedel systems share the Laguna del Maule as a depocenter and create a positive feedback for their related deformation areas.
- Remote sensing methods for lineament extraction to envisage the tectonic processes fingerprint on the Earth surface.
- The drainage pattern and channel direction provide information on tectonic processes

Abstract

The tectonic movement along faults is often reflected by geological lineaments, appearing as geomorphological features caused by relief. The detection and quantification of geological lineaments raises interest as it provides information on tectonic processes. During the last decade, remote sensing data has been used as a source of information for the detection of geological lineaments; however linear features acquired via different GIS techniques are usually not consistent. Based on the drainage pattern, this study provides a new approach to envisage the tectonic footprint on the Earth surface, that has been successfully tested and compared with field structural characterizations. The tectonic framework of the Laguna del Maule Volcanic Complex (LdMVC), in the Southern Andean Volcanic Zone, is distinguished by local structural domains characterized by diverse but coherent fault geometries and kinematics that accommodate bulk crustal deformation, coexisting with high local uplift rates related to magma ascend. The analysis of local lineament populations suggests the interaction between two conjugate Riedel systems sharing the LdMVC as a depocenter: An orogenic scale dextral system, that has favored the formation of wide ENE oriented extensional areas, is intersected by another sinistral WNW-NW Riedel system, likely favored by the reactivation of ancient Andean transverse faults (ATF). The coexistence of both Riedel systems creates a positive feedback for their related deformation areas, and therefore, favoring the formation of intense damage zones, which in turn, promote the structural conditions for the migration and emplacement of magma and geofluids.

Plain Language Summary

The study of tectonic structures raises a high scientific interest as it controls the location of mineral deposits and has a direct relationship with geological risks. Remote sensors are a booming tool that today allows us to make large-scale measurements and analysis of the Earth's

surface relief. Some geomorphological characteristics of the relief, such as the spatial distribution of ridges and rivers that conform the drainage network, can be related to tectonic processes. This study presents a new approach that allows to recognize tectonic processes from the orientation of rivers and streams. The method has been tested and presents surprising results in the Laguna del Maule Volcanic Complex, one of the most hazardous active volcanic systems on the Southern Andean Volcanic Zone.

1 Introduction

1.1 The Laguna del Maule Volcanic Complex (LdMVC)

The Southern Andean Volcanic Zone (SAVZ) displays remarkable along-strike structural variations (e.g., Cembrano and Lara, 2009). Stratovolcanic complexes, minor eruptive centers, and geothermal springs are roughly aligned and appear to be emplaced on morphostructural lineaments, that represent second-order structures acting as magma and fluid pathways. These morphotectonic features have been categorized into two groups according to their strike: NW to WNW striking structures, named Andean Transverse Faults (ATF), and ENE transtensional subsidiary faults (e.g., Cembrano and Lara, 2009; Pérez-Flores et al., 2016). The geomorphic expression of this structures can be easily observed from remote sensing (e.g., Reyes-Wagner et al., 2017), but its quantification and interpretation remains little studied.

The LdMVC, in the intra-arc of the SAVZ at 36°S (Figure 1), presents a complex tectonic framework that has acquired scientists interest due to the large surface uplift rates detected by satellite geodetic measurements since 2007 (Feigl et al., 2014; Fournier et al., 2010; Le Mével et al., 2015; Singer et al., 2018). Although no historic eruptions are associated to the LdMVC, large volume of Holocene silicic volcanism have been recognized along the volcanic

field (Hildreth, 2010; Singer et al., 2014). The LdMVC includes >130 volcanic vents over ~300 km2 that have produced ~13 km3 of postglacial rhyolitic eruptions (Andersen et al., 2017). This, combined with the large uplift rates, convert the LdMVC as one of the most hazardous active volcanic systems on the SAVZ. Cycles of magmatic uplift occurs over decadal to centennial timescales, and faults in and around the resurgent area are nucleated and reactivated to accommodate the inflation-driven deformation (e.g., Acocella et al., 2004; Levy et al., 2018). The structural characterization of tectonic deformation in resurgent systems is challenging because their faulting record encompasses tectonic and inflation-driven deformation. Rapid inflation rates above silicic reservoirs result in concentric uplift patterns that mask tectonic extension in geodetic measurements (e.g., Le Mével et al., 2016; Magee et al., 2010).

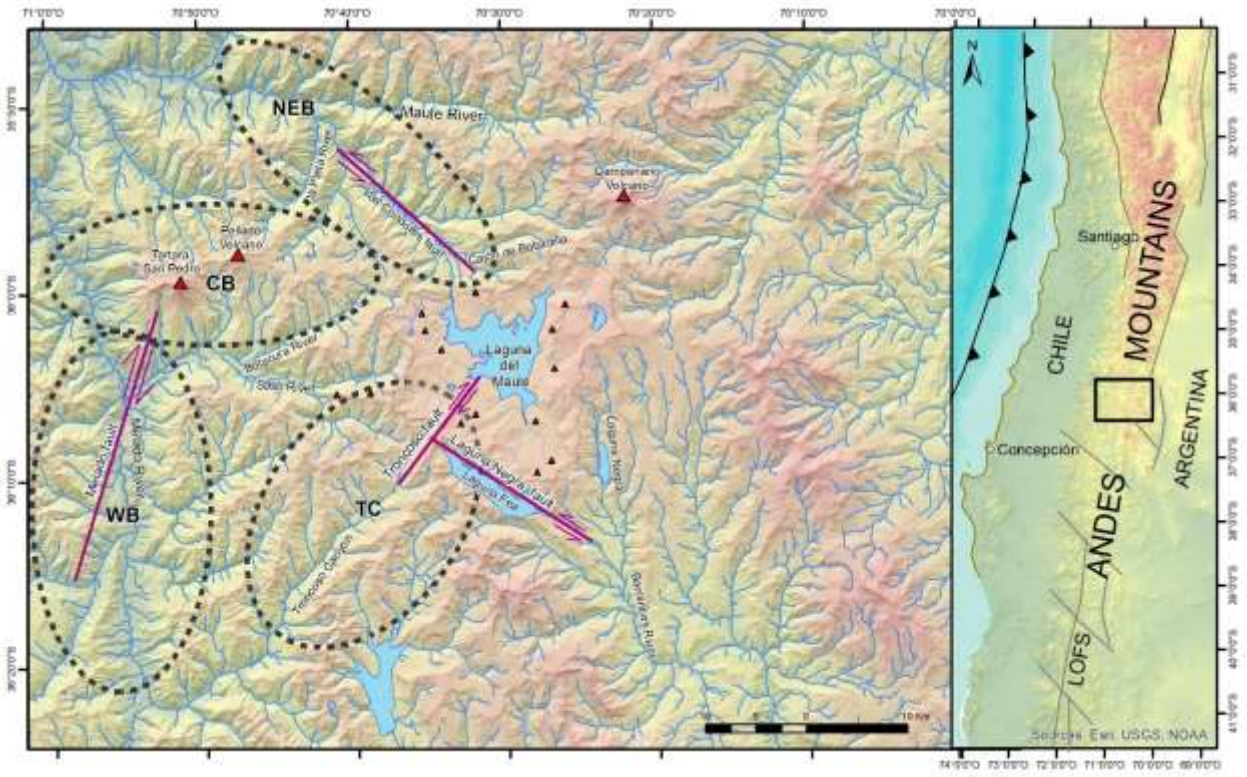

Figure 1. Digital elevation model of the study area, centered on the LdMVC. The map with the river network superimposed shows the name and location of some places referred in the text. The Ellipsoids represent the four subdomains where the method has been tested and compared with field measurements. They are identified as CB, NEB, WB and TC. At the right side, the location of the study area within the Andean range.

1.2 Lineament extraction from remote sensing

The spatial pattern of geologic structures, such as faults or dykes, and related morphological lineaments, is characteristic to the stress field causing tectonic deformation (Keller and Pinter, 1996; Ramsay and Huber, 1987). Large continuous lineaments are often the direct surface expression of deep structures so that, linear tectonic landform could be used to trace down fracture zones. (Han et al., 2018; Jordán et al., 2005; Solomon and Ghebreab, 2006; Soto-Pinto et al., 2013; Tripathi et al., 2000). It is widely accepted that regional strain is partitioned heterogeneously within fault systems, with local structural domains characterized by diverse but coherent fault geometries and kinematics, which accommodate bulk crustal deformation. Tectonic strain introduces directionally dependent characteristics of rock displacement and damage, both of which influence the pace of geomorphic responses (Molnar et al., 2007; Roy et al., 2016).

Geologic lineaments are clearly discernible on the Earth's surface. Remote sensing techniques provide additional information on the spatial arrangement and distribution of faults and fractures in large areas, with variable outcrop conditions (e.g., Flores-Prieto et al., 2015; Grohmann, 2004; Hashim et al., 2013; Jordan and Schott, 2005; Soto-Pinto et al., 2013). In the

last decades, remote sensing data has been used as a source of information for the detection of tectonic structures at a regional scale. Different methods of extracting lineaments from satellite images (Jordán et al., 2005; Marghany and Hashim, 2010; Suzen and Toprak, 1998) and Digital Elevation Model (Abdullah et al., 2010; Grohmann, 2004; Masoud and Koike, 2017) have been proposed and tested worldwide. Several studies have compared diverse data source, methods and algorithms applied to the same study area, however, their results are usually inconsistent (Adiri et al., 2017; Farahbakhsh et al., 2020; Han et al., 2018; Hung et al., 2005; Koike et al., 1998; Meixner et al., 2018). Currently, most researchers apply multi-scale edge detection, as the spatial distribution frequency and length of lineaments depends on the data source (Liu et al., 2019; Radaideh et al., 2016), on the observation scale (e.g., Barth et al., 2012; Xu et al., 2020), or on the spatial resolution (Das and Pardeshi, 2018; Meixner et al., 2018; Rajasekhar et al., 2018; Smith and Wise, 2007; Soliman and Han, 2019).

Drainage network patterns tend to reflect the geometry of underlying active or inactive tectonic structures due to the rapid erosion of faults and differential uplift associated with fault motion (Castelltort et al., 2012). Drainage pattern is somehow controlled by regional tectonic stress field (e.g. Beneduce et al., 2004; Duvall et al., 2020; Ribolini and Spagnolo, 2008; Roy et al., 2016; Shahzad et al., 2009). However, the relationship between channel orientation and tectonics is not well constrained yet, and whether these patterns contain fingerprints of past tectonic events is still debated (e.g., Gioia et al., 2018; Hodgkinson et al., 2006; Perron et al., 2012). The reason is that rivers are dynamic entities capable of independent lateral incision, and dynamic reorganization along time (e.g., Babault et al., 2012; Bishop et al., 2005; Brocard et al., 2011; Guerit et al., 2016; Pastor et al., 2012). Many rivers in active mountain belts rapidly

evolve in response to tectonic deformation, while others seem to be passive features and may record long-term crustal deformation (Castelltort et al., 2012).

The mapping and interpretation of tectonic lineaments is very complex and requires the inspection and integration of the geological and geomorphological features of the target area. This study presents simply criteria to use the drainage network pattern as a tectonic footprint. We propose a step-by-step procedure, based on the Strahler hierarchical order (Strahler, 1964), in order to enhance the directionality of the drainage pattern related to structural control. This method has been tested in the intra-arc of central Andes, at latitude 36° S, where structural field work with hundreds of field measurements characterizing the San Pedro – Pellado and the Laguna del Maule Volcanic Complex (SPPVC and LdMVC) has been recently published (Cardona et al., 2018; Garibaldi et al., 2020; Sielfeld et al., 2019b).

2 Materials and Methods

In recent years, most studies on the extraction of geological lineaments from remote sensors have focused on improving the algorithms for the extraction of lines from raster datasets. In this study only the drainage pattern shape is considered as a strain marker and it is used to infer hidden tectonic structures. This approach reduces the number of extracted lines with respect other methods, as most of them are considered redundant information.

Here, we propose a methodology to enhance the tectonic signal present in the drainage pattern, based on the Strahler hierarchical ordering of drainage channels (Strahler, 1964). We perform a different geostatistical treatment on different order segments, giving higher weight to higher order segments, commonly related to tectonic structures, without dismiss the lower order

segments, assigned to a lower weight in the directional statistics. The process is resumed in the flowchart of Figure 2, and it is also fully described below.

The proposed method was tested in the areas outlined in Figure 1, where previous structural studies provide hundreds of field measurements (Garibaldi et al., 2020; Sielfeld et al., 2019b). Following these studies, the subdomains of Troncoso Canyon (TC), San Pedro Pellado volcanic complex (BC), the Wester block (WB), and the North Easter block (NEB) are adopted here. Once the method was calibrated in areas with detailed structural characterizations, the study area was expanded to carry out a regional scale study. For this purpose, a grid, separating the entire study area in 16 subdomains of 425 km2 each, was generated and individual analysis were performed to derive the directional trending in each subdomain, that are finally represented in rose plots.

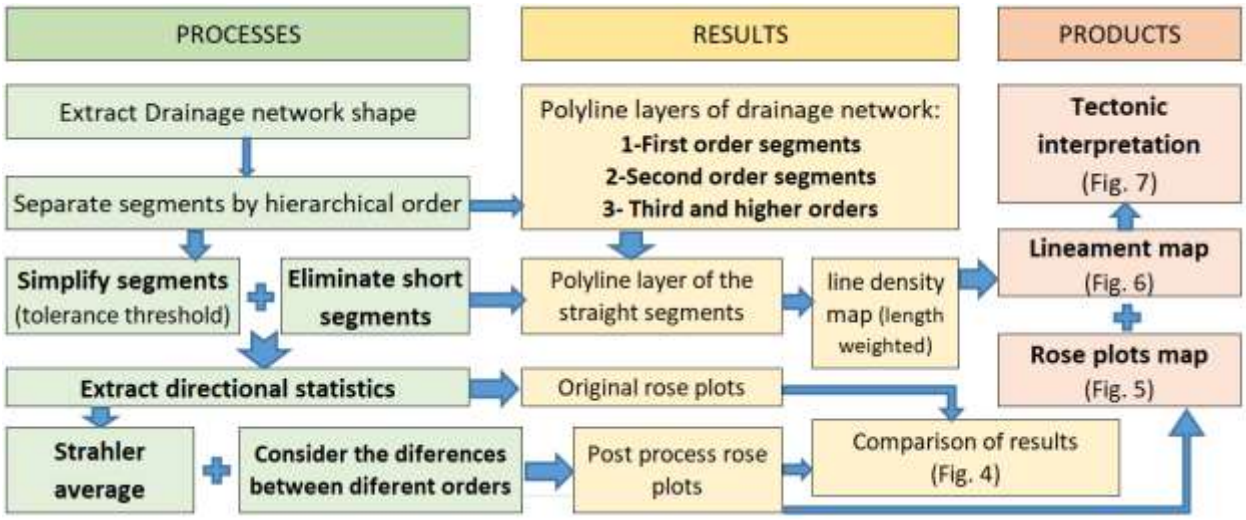

Figure.2 Flow chart with the steps to follow in the methodology of this study

2.1 Derive drainage network and Strahler order

The drainage network is an interconnected pattern of dry gullies formed by water erosion along with streams and main rivers. In this study, the drainage network was derived from the ALOS PALSAR DEM (12,5 m), based on the D8 (multidirectional method) method using "Hydrology Tool" (Tarboton et al., 1991) in ArcGIS software 10.3 version. The D8 model algorithm determines the flow direction based on water flow from a given cell into only one adjacent cell. The flow accumulation was calculated from the flow direction raster by assigning a threshold area (Jenson and Domingue, 1988). River networks are then derived by imposing a variable threshold for the minimum contributing area, which value finally determines the drainage densities (e.g., Colombo et al., 2007). However, the distribution of azimuth directions for the drainage networks at various threshold levels derives not significantly different results (Radaideh et al., 2016). In this study, an accumulation threshold of 1600 DEM cells (0,25 km2) was used as a routine criterion.

On the other hand, Strahler stream ordering system (Strahler, 1964) reflect morphometric parameters of the drainage network and depends on the drainage density, which in turn depends to the minimum contribution area threshold used to extract the drainage network. Strahler order can be derived from digital elevation data by using specific GIS tools. Recent studies demonstrate how the direction of the drainage network and its relation with tectonics varies with the Strahler orders (e.g., Duvall et al., 2020; Resmi et al., 2019; Saidi et al., 2020). In this study, we first separate and then focus on the directional properties of 1) 1st order channels, 2) 2nd order channels, and 3) channels of 3rd and higher orders.

171 ## 2.2 Segment simplification process

172 The drainage network is composed by sinuous lines that need to be broken up in straight
173 segments, in a process called simplification. For this purpose, the Douglas-Peucker algorithm
174 (Douglas and Peucker, 1973) is used in order to reduce the number of points needed to represent
175 each river segment to within a certain predefined tolerance. The tolerance is the maximum
176 distance that any point (vertex) of the original river path can be laterally separated from the
177 straight line that best fits the original river segment. A smaller tolerance distance generates more
178 well-fitted straight segments to the original rivers, while using a larger tolerance the drainage
179 network becomes over simplified and less straight segments are needed to represent it. The effect
180 of increase the tolerance is similar to reduce the resolution of the data source, resulting in larger
181 straight segments from the simplification process (e.g. Barth et al., 2012).

182 The tolerance threshold must be defined according to the geomorphic characteristics of
183 river network. A drainage network study using Google Earth showed quite straight rivers in the
184 main valleys (sinuosity index <1.2), with some local sinuosity due to endogenic dynamic
185 processes, such dejection cones reaching the channel from the lateral hillslopes, lava flows
186 locally changing the hardness of the valley floor, or sections where the river follows a
187 meandering path. On the other hand, first-order segments generally appear as streams embedded
188 in the slopes, with very little lateral mobility. Therefore, we simplify the first order segments
189 using a tolerance range of only 75 meters, whereas a tolerance range of 300 meters wide has
190 been granted in the simplification process of rivers of third to sixth order. Then a threshold of
191 150 m is assigned to the second order channels after applying the principle of linear progression
192 of tolerance.

193 ### 2.3 Extract length and frequency statistics

194 Once the drainage network is classified and separated by channel ordering, and sinuous
195 segments are simplified to straight segments using different tolerance thresholds, short segments
196 are eliminated by segment debugging. The criteria used to remove short segments again varies
197 according to the Strahler order, as all segments with length less than twice the tolerance value
198 occupied were debugged in the line simplification process. The effect of removing the short
199 segments on the statistic is that the mean length of the remaining segments become larger, as the
200 number of segments is significantly reduced while the total length is almost not affected.

201 Using specific GIS tools, we extract the values of direction and length for all segments
202 composing a polyline layer. In this study, separated statistics of channel directionality for
203 segments of the first, second, and higher hierarchical orders were extracted. The results include
204 the total length and frequency of straight segments for a given interval of direction (e.g. 18 bins
205 of 10°).

206 The total length of segments in a given direction –instead of the number of segments- has
207 been used in the statistics to follow, and therefore, rose plots are length weighted. The mean
208 length of the rectilinear segments is considered a fundamental parameter to define tectonic
209 lineaments (e.g., Han et al., 2018; Saidi et al., 2020).

210 ### 2.4 Strahler averaged directions

211 The interrelation between the drainage network and tectonics differs between segments of
212 different Strahler orders (e.g., Resmi et al., 2019; Saidi et al., 2020). As a general rule, segments
213 of higher orders are more controlled by main tectonic structures, whereas segments of the lower
214 orders are more affected by noise (e.g., Duvall et al., 2020; Gioia et al., 2018). Based on this, we

would only use the higher order segments to analyze the directionality of the drainage network. However, the total length of the third or higher order segments is only the 25% of the total length of the entire drainage network (see Figure 3), and the other 75% of segments would contain valuable information at a local scale.

After the extraction of the directional statistic data for three hierarchical orders (Figure 4) the total length in all directions to 100%, in order to obtain the percentage of the length of segments in each direction. This normalization process allows comparing the directionality of different Strahler orders segments, independently of the differences in their total length. Then, the normalized percentages were used to carry out an average from the results of the three hierarchical orders, in each zone.

$$\text{Strahler average for direction}_i = (\text{percent order1}_i + \text{percent order2}_i + \text{percent order3}_i)/3$$

This averaged percentage implicitly carries a weighting operation, here called the "Strahler average". The Strahler average is conditioned by the Strahler length ratio (Strahler, 1964), which relate the total length of segments of a given order with respect to the total length of the segments of the next higher order. For example, in the focus area of this study, segments of order 1 double the total length of those of order 2, being the length ratio close to 2. Thus, when average the normalized percentages for each direction (separated directional analysis for different Strahler orders), channels of higher order-which have a shorter total length- get a greater specific weight in the averaged percentages. The sub process named "Strahler average", where the normalized percentages are averaged, implies that the specific weight of a certain order segments in the average is inversely proportional to the total length of the river segments in that order.

The last statistical manipulation is applied to enhance the directions related to tectonic structures. It is assumed that, when a channel is following a tectonic structure, most tributaries will be perpendicular or oblique to it. Therefore, if channels of different orders follow the same direction, it would be assumed that this is probably due to the regional slope. Here we propose to consider the deviations between individual analyses – percentages of segments in the same direction, for the different Strahler orders- with respect to their average. Deviations are added, as an absolute value, to the Strahler average (SAv).

Final % for direction$_i$ = %SAv + ABS (%SAv - %order1$_i$) + ABS (%SAv -%order2$_i$) + ABS (%SAv -%order3$_i$)

2.5 Density map and lineament interpretation

The density map was performed from the shape conformed of straight segments, representing the original drainage network, using the "line density" algorithm of ArcGis. For this process, a search radius of 0.5 km was used, and the segment length was applied as a weighting value. As a result, river paths have different density signal depending on the length of the straight segments. Finally, a manually draw of the lineaments was performed by following the highest density spots, which correspond to the longer straight segments of the fluvial network. The lineament map is finally used to perform the tectonic interpretation.

3 Results

3.1 Strahler order, segment length and frequency

In the 6500 km2 study area, the total length of drainage network (upstream catchment> 0.25 km2) is about 12900 km. After the simplification process, the data has been filtered to eliminate the shorter segments with lengths being less than the width tolerance previously used

to simplify lines. The reduction of shorter segments leads to a total length of 7830 km, that is the value considered for further analysis.

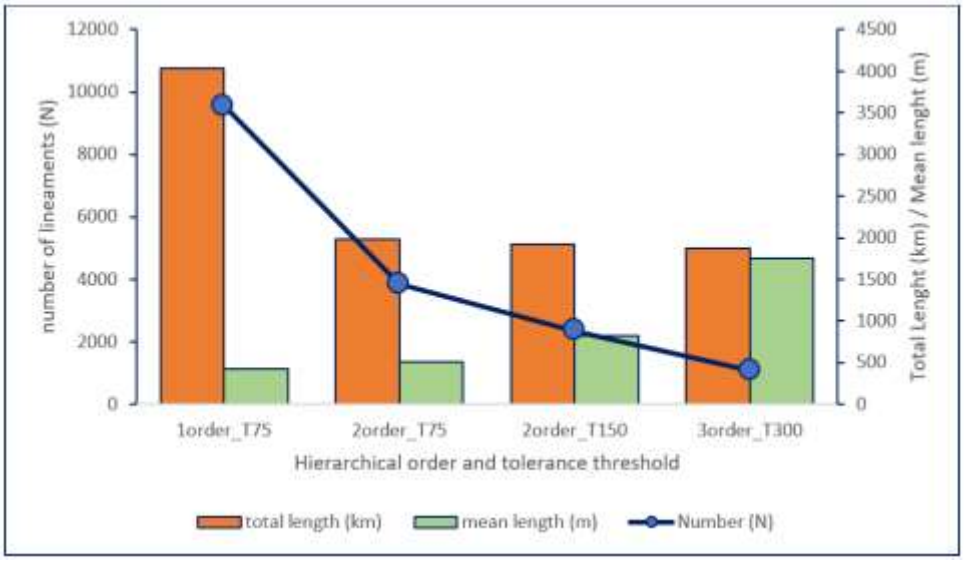

Figure 3. Graph showing the differences in the number of straight segments, total length, and mean length derived from the drainage network of the entire study area, and separated by different Strahler orders. Note that different threshold values of tolerance were used in the simplification process. The first columns represent the first order segments, which were simplified with a tolerance of 75 m. The second columns represent the second order segments and the same tolerance of 75 m., whereas the third column are the second order segments obtained with a tolerance threshold of 150 m. The fourth column are the third to sixth order segments, using a tolerance threshold of 300 m.

The figure 3 illustrates the influence of the Strahler order and simplification tolerance threshold on the number of segments, their mean length, and the total length. The comparison between first and second column (Figure 3) show the difference in number and length between

first and second order segments, when both were simplified using the same tolerance threshold (75 m). The total length of second order segments is about 60% less than first order segments (from 9554 to 3863 km), what means a length ratio of 2.5 approx. In such case, the mean length of segments does not vary significantly between first and second order (from 423 to 511 m.). On the other hand, the comparison between the first and third columns (Figure 3) show that the mean length of segments increases by 160% (from 511 to 822 m) when a wider tolerance (150 m) is used to simplify the second order segments. In this case, the number of second order segments is about 25% of the number of first order channels, whereas the total length decreases about 50% (length ratio ≈ 2). Consequently, the mean length of the second order segments is almost twice the mean length of the first order segments (from 423 to 822 m.). The third to six orders segments (fourth columns in Figure 3) present a total length similar to the second order segments, being the consequent relation considering a length ratio close to 2. From these observations, we recognize how the tolerance threshold used in the simplifying process affects to the length ratio, which is determined by the difference in the total length between two consecutive Strahler orders.

3.2 Drainage network directions

The view of different plots representing the directionality of the drainage network allows to compare the differences and similarities between the different approaches (Figure 4). The same analysis was performed for the entire study area, and for four subdomains (see locations in Figure 1), where recent studies provided detailed structural data from field measurements (Garibaldi et al., 2020; Sielfeld et al., 2019).

The representation of the first order segments create the most homogenous rose plots, especially in larger areas (Figure 4). As first order segments greatly contribute to the total length

297 of the drainage network (50% of the total segment length), the complete drainage network
298 directionality -before any treatment- also show very homogeneous roses, with no clear
299 preferential trends. (fourth column in Figure 4). Segments of different orders present different
300 main directions (Figure 4). As a general observation, the main direction of second order
301 segments is almost perpendicular to the main direction of the segments of third and higher
302 orders, whereas the main direction of first order segments appears parallel to the second order
303 segments in some locations, and oblique to perpendicular in others.

304 The analysis of the entire study area (first row in Figure 4), show the first and second
305 order channels represented with homogenous roses, whereas the segments of higher orders show
306 a light trend to the NNW. By contrast, smaller areas present clear trends standing out in most
307 rose plots, even those representing the first order segments (Figure 4).

308

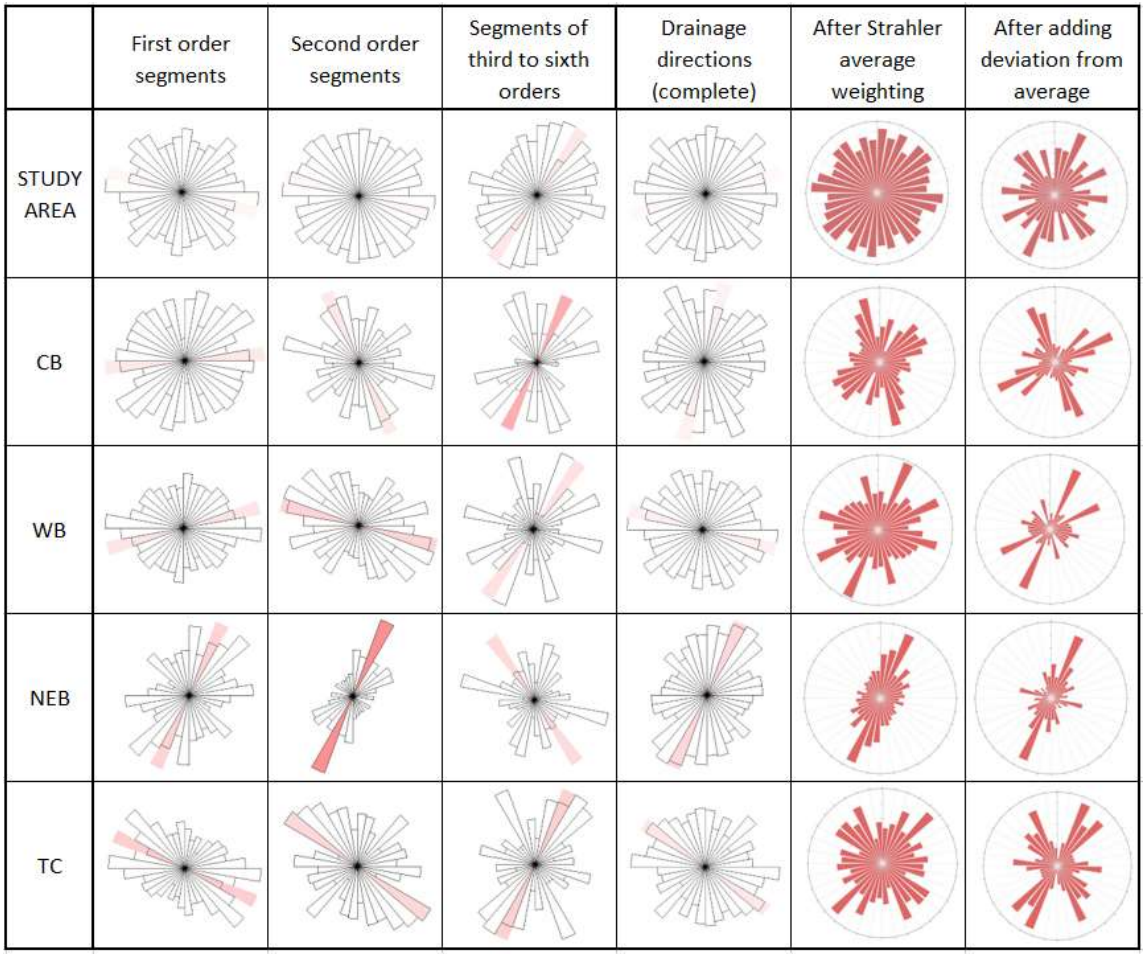

Figure 4. Rose plots with 10° bins showing the directionality of the drainage network (all length weighted), with the circular mean direction shown as a light red bin. The rose plots in the first three columns shows the directionality of the drainage network, separated for the first, second, and third to sixth order segments. Plots in the fourth column show the directionality of the the complete drainage network (>0.25 km2 upstream), before any treatment. Plots in the fifth column shows the directionality after the Strahler average weighting; and plots in the sixth columns shows the final results, after considering the relative differences between segments of different Strahler orders.

The rose plots after the Strahler average and after considering the deviation from the average (columns 5 and 6 in Figure 4) show the effect of the post-process carried out to enhance the directions of the drainage network related to tectonic structures. The rose plots in the column "Strahler average" show the effect of enhancing the directionality of the higher orders with respect to first order segments. Finally, the rose plots at the outmost right column are the result of considering the directional differences between channels of different hierarchical order, which allows enhancing the directions that stand out in a specific Strahler order, even when such direction do not stand out in average. The last enhancing effect is particularly notorious in the results considering the whole study area.

3.3 Drainage directions Vs. structural measurements

In order to test the proposed method, the directionality of the drainage network was determined for the entire study area, were the main tectonic trends at an orogenic scale is expected to be detected. These results were also tested in the 4 subdomains within the study area (Figure 1), where previous detailed structural characterizations have been recently published. The results of the analysis of the drainage pattern according to the presented methodology are full in line with the field measurements.

The final rose plot of the entire study area (right column; Figure 4) presents four main trends that stand out from the average: 1). The NNW direction, parallel to the plate margin, is the dominant trend, and coincides with the main structures along southern Andes (e.g., Liquiñe-Ofqui fault system). 2) Almost perpendicular to the main trend, the NW-SE direction is related to the Andean Transverse Faults (ATF), which have been broadly recognized at southern latitudes (e.g., Cortaderas lineament; Cembrano and Lara, 2009; Sielfeld et al., 2019a), and also north of the study area (e.g., Tinguiririca fault; Giambiagi et al., 2019; Pearce et al., 2020). 3) The third

direction standing out is the 60-70° ENE trend, coinciding to the structural anisotropy named the Tatara Damage Zone (TDZ) (Ruz et al., 2020; Sielfeld et al., 2019b). 4) Finally, the E-W direction (90-100°E) also stand out.

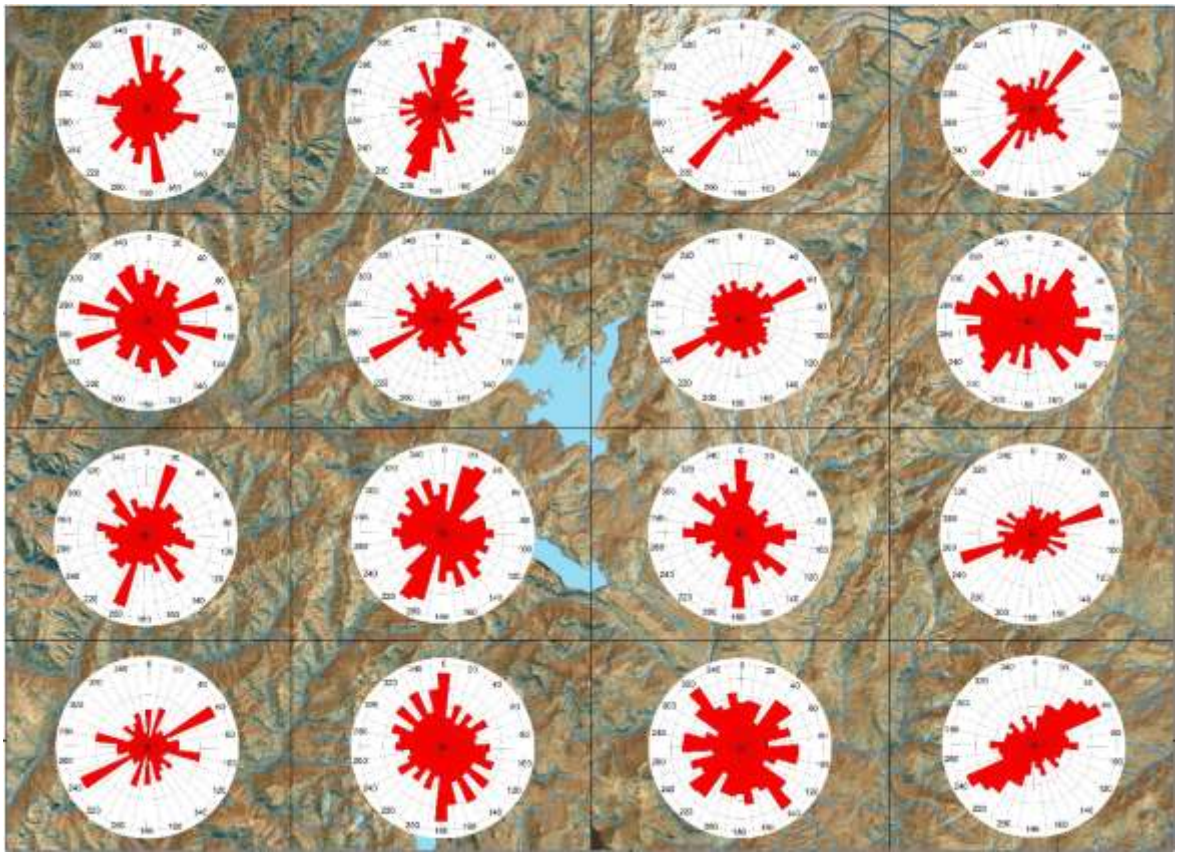

Figure 5. Map of the study area divided in 16 subdomains. Rose plots show the directionality of the drainage network after the statistical post process.

The first subdomain used to test the method is centered in the Tatara - San Pedro Volcanic Complex (CB; Figure 1), an Early Pleistocene–Holocene group of composite volcanoes, lava flows, dike swarms, and minor volcanic vents, with a general ENE orientation (Singer et al., 1997). This area is characterized by dominant ENE- to WNW-striking normal faults (Sielfeld et al., 2019b). The post-processed rose plot (right column, Figure 4) shows a

predominant direction of 60-70° (ENE), and 100-110° (WNW). The NNW-SSE also stands out in the plot (Figure 4), related to the main rivers in the area (Melado and Colorado rivers), and also minor canyons draining the north face of the San Pedro volcanic edifice (Figure 1). Structures striking NNW has been reported in the western edge of this domain (see Figure 3 in Sielfeld et al., 2019b), and this direction coincides with the stress condition for the orientations of all pre volcanism dikes, placed in a tensional regime (Sielfeld et al., 2019b). The NE trend also appears as a large petal in the rose plot, and it is probably related to the NE-striking La Plata Fault.

The Western Block (WB; Figure 1) is defined by volcano-sedimentary rocks affected by NNE- to ENE-oriented transtensional dextral oblique-slip faults (Sielfeld et al., 2019b). The directionality of the drainage network in this area fully matches the field observations (Figure 4). The NNE direction is related to the Melado fault, which presents recurrent seismicity at its northern edge, near the southern slope of the Tatara-San Pedro volcanic complex (Cardona et al., 2018). On the other hand, the N 60-70° E is related to the TDZ and its associated structures (Sielfeld et al., 2019b).

The Northeastern Block (NEB; Figure 1), located along the Maule and Los Condores valleys, to the northwest of the LdMVC, present a very dominant NNE direction, probably related by La Plata fault, which follow a well-recognized lineament striking N25-20°E. The predominance of the NNE direction is particularly notorious at second order channels (Figure 4). The secondary trend is the 100°E probably related to the Maule Valley lineament. By contrast, the NW-striking structures recognized in the field (e.g. Los Condores fault; see Sielfeld et al., 2019b) does not stand out within the drainage main directions in this area.

The Troncoso Canyon (TC; Figure 1) is characterized by the Troncoso fault, a major normal fault that strikes NE and dips to the NW. The Troncoso hanging wall contains abundant, young (b 23 ka) NE-striking normal faults, whereas the footwall is largely unfaulted, with few NNW-striking faults (Garibaldi et al., 2020). Similarly, the analysis of the drainage network in this area shows the NE-SW as the main direction, and the perpendicular NNW-SSE direction appears as the secondary main trend. The E-W direction slightly stand out in the rose plot (Figure 4), and such direction was recognized as the main direction for strike slip structures in the Troncoso Canyon (Garibaldi et al., 2020). The 40-50° NE direction predominates in subdomains located to the NE of the study area (Figure 5).

In summary, four main direction stand out from the drainage pattern in the study area: NNE-SSW, NW-SE, ENE-WSW, and E-W (Figure 5). The newly proposed statistical approach to interpret the directionality of the drainage network fully matches the field observations in the whole area and minor subdomains. This coincidence demonstrate that the processing proposed in this study helps to enhance the directions of the drainage network related to tectonic structures.

Finally, a line density map, derived from the straight segments of drainage network, was used to perform a lineament map (Figure 6), which in turn, was used to infer tectonic structures and interpret the tectonic setting. (Figure 7).

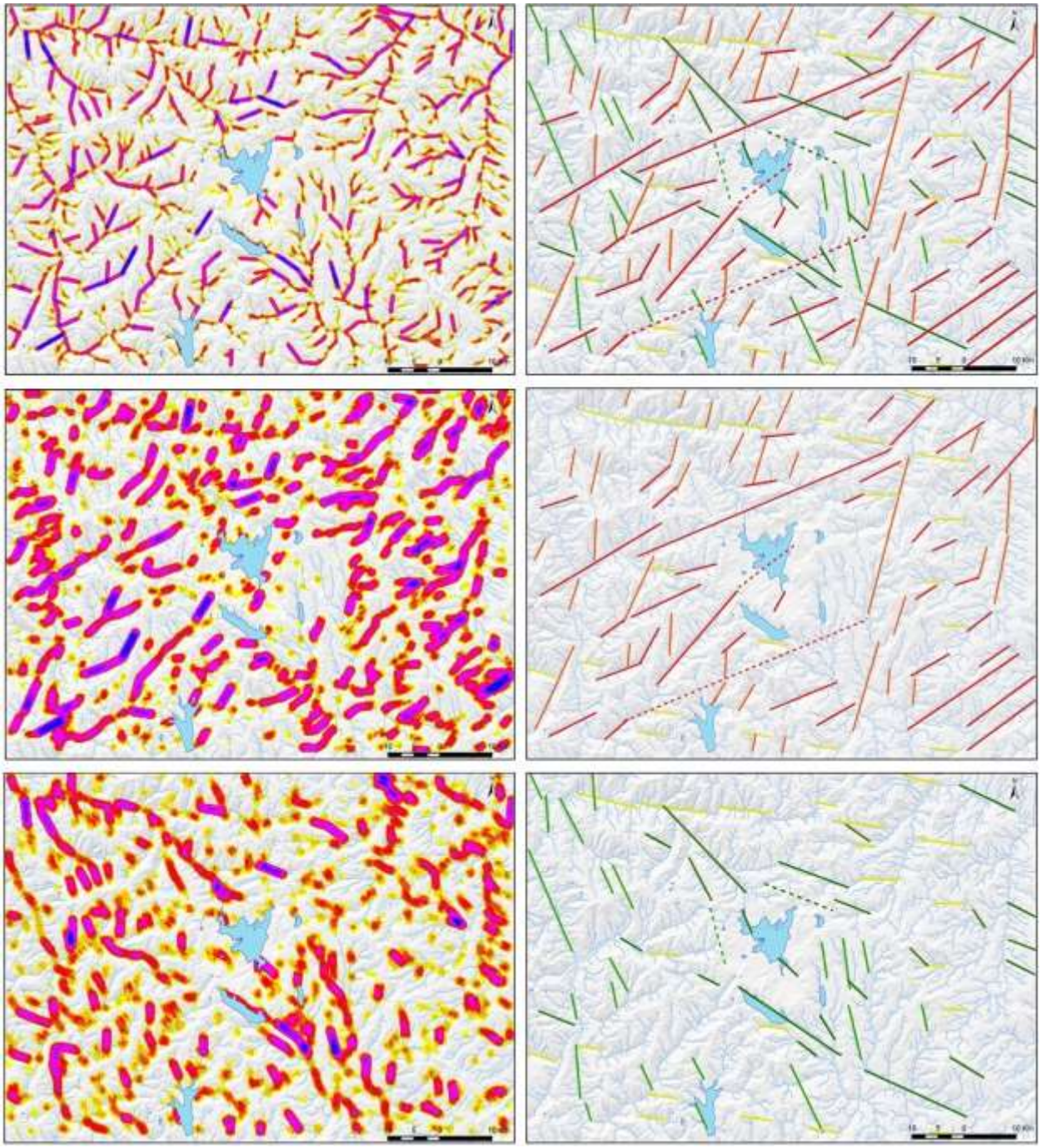

Figure 6. Line density maps (left column) and their interpretation (right column), resulting in lineament traces. The upper map presents the density result of all the straight segments composing the drainage network. The middle and lower maps only plot segments oriented in 0-90°N, and 90-180°, respectively. Colors of lineament only represents different directional ranges.

4 Discussion

4.1. Tectonic evolution from lineament interpretation

Crustal deformation derived from plate convergence is heterogeneously accommodated within fault systems in the intra-arc region of the Southern Andes, where local structural domains are characterized by diverse but coherent fault geometries and kinematics. The SAVZ is of particular interest due the long-term mechanical interaction between NNE striking margin-parallel faults and the Andean Transverse Faults (ATF) trending WNW-NW (e.g. Cembrano and Lara, 2009; Rosenau et al., 2006). At orogenic scales, this interaction results in Riedel-type deformation, favoring the formation of ENE oriented transtensional fault damage zones, which in turn, facilitate structural conditions for the migration and emplacement of geofluids in the upper crust (Pérez-Flores et al., 2016; Sielfeld et al., 2019b; Stanton-Yonge et al., 2016).

The analysis and interpretation of the drainage pattern in the LdMVC area suggest the interaction of two conjugate Riedel systems, both characterized by extensional and compressional areas delimited by strike slip faults. The Melado Fault, at the eastern edge of the study area (Figure 1), is a strike-slip fault striking N to NNE, here considered as the master western fault of a dextral Riedel system (Figure 7A). North of the study area, the E-W lineament following the Maule valley is related to a sinistral strike-slip fault, which would correspond to a type R' antithetical fault of a Riedel system. Other E-W lineaments can be inferred at the center and south of the study area (yellow lines in Figure 6). The Troncoso Fault, which crosses the Laguna del Maule in a NE-SW direction, is defined as a dextral strike-slip fault with a normal component (Garibaldi et al., 2020), and would be interpreted as a R-type synthetic fault of a Riedel system.

The dominant ENE trend within drainage patterns is related to the Tatara Damage Zone (TDZ). This trend is also found within a wide area south to southeast of the LdMVC (Figure 5), where extensive volcanic formations, from the Miocene to the recent period, have been documented (Narciso et al., 2004). The TDZ is characterized by the generalized presence of ENE-striking normal and strike-slip faults, combined with the emplacement of dike swarms oriented 60-70°E, since the early Pleistocene (Sielfeld et al., 2019b). The geometry and location of the TDZ is compatible with the extension zones in a Riedel system (Figure 7). This broad extensional region is related to distinct magma bodies, associated with the Tatara-San Pedro and the Laguna del Maule volcanic complexes, and the Mariposa Geothermal System (Reyes-Wagner et al., 2017; Sielfeld et al., 2019b). The lineament map generated in this study (Figure 6) allows to extend the TDZ to the E, as far as up to the Campanario Volcano (Figure 7).

The drainage network tends to reflect the geometry of underlying active or inactive tectonic structures, so passively deformed and dynamically rearranged river basins may coexist in the same mountain range (Castelltort et al., 2012). In order to explain the tectonic evolution of this area, the E-W Maule valley lineament is interpreted as an ancient ATF, which was a dominant fault prior to the progressive rotation of the compressional vector, occurred since the Pliocene (Lavenu and Cembrano, 1999; Pardo-Casas and Molnar, 1987). This progressive rotation in the stress field may favor the development of dextral strike slip and normal ENE-striking faults within the TDZ. The ENE direction also coincides with the presence of normal faults located in the northern margin of the Laguna del Maule (Cajón de Bobadilla), previously defined as a series of collapse structures generated after old mega eruptions (Hildreth, 2010). Finally, the tectonic framework favors the development of an ENE oriented transtensional pull apart basin, with the Laguna del Maule as a depocenter (Figure 7B). Similar structures have been

observed in analog models (Wu et al., 2009). Then, the Troncoso fault is considered as the main exponent of the cross-basin strike slip fault zone. Additionally, the recent development of en-echelon oblique-extensional faults close the Laguna Negra, to the west of the Laguna del Maule, have been identified. These structures are characteristic transtensional pull apart basins (Wu et al., 2009).

Simultaneously to the development of the pull apart basin, the adaptation to the new stress field probably led to the gradual decrease in the amount of deformation accommodated by the main E-W sinistral faults, and the reactivation of other faults with sinistral kinematics, in a NW-WNW to SE-ESE direction (e.g. Los Cóndores and Laguna Fea faults). The reactivation of ancient ATF faults is also suggested by Pearce et al., 2020 for the Tinguiririca Fault, located about 100 km to the north of the study area. The current seismicity along the Laguna Fea Fault (see Cardona et al., 2018) and the identification of others NW-WNW striking lineaments located northwards is consistent with the development of a conjugated sinistral Riedel system. Within this second set of Riedel structures, the long-lived NE striking Troncoso Fault is acting as a dextral strike-slip fault, corresponding to a type R 'sinthetical fault of a sinistral Riedel system. The R-type antithetical fault of this system would be represented by an incipient E-W lineament, crossing close to the southern margin of the present lagoon, what is consistent with the presence of E-W strike slip faults recognized in this area (Garibaldi et al., 2020), and also westward, in the Saso Canyon (Sielfeld et al., 2019b).

The orogenic scale dextral Riedel system and the local sinistral Riedel system share the LdMVC as a depocenter (Figure 7B). Fault geometry support the interpretation that active faults at the LdMVF are tectonic rather than volcanic in origin, forming a transtensional zone that hosts the magmatic system (Peterson et al., 2020). The interaction between conjugate Riedel systems,

sharing the Laguna del Maule as a depocenter, is consistent with the normal component of the Troncoso Fault, and the recent SW-NE and N-S faulting (Garibaldi et al., 2020; Peterson et al., 2020). The occurrence of a minor scale pull apart basin, having the Troncoso fault as the western master fault, has been suggested by other authors (Cardona et al., 2018; Miller et al., 2017), however at the scale of the present study, it is not detected from drainage patterns in a 12.5m X 12.5m DEM.

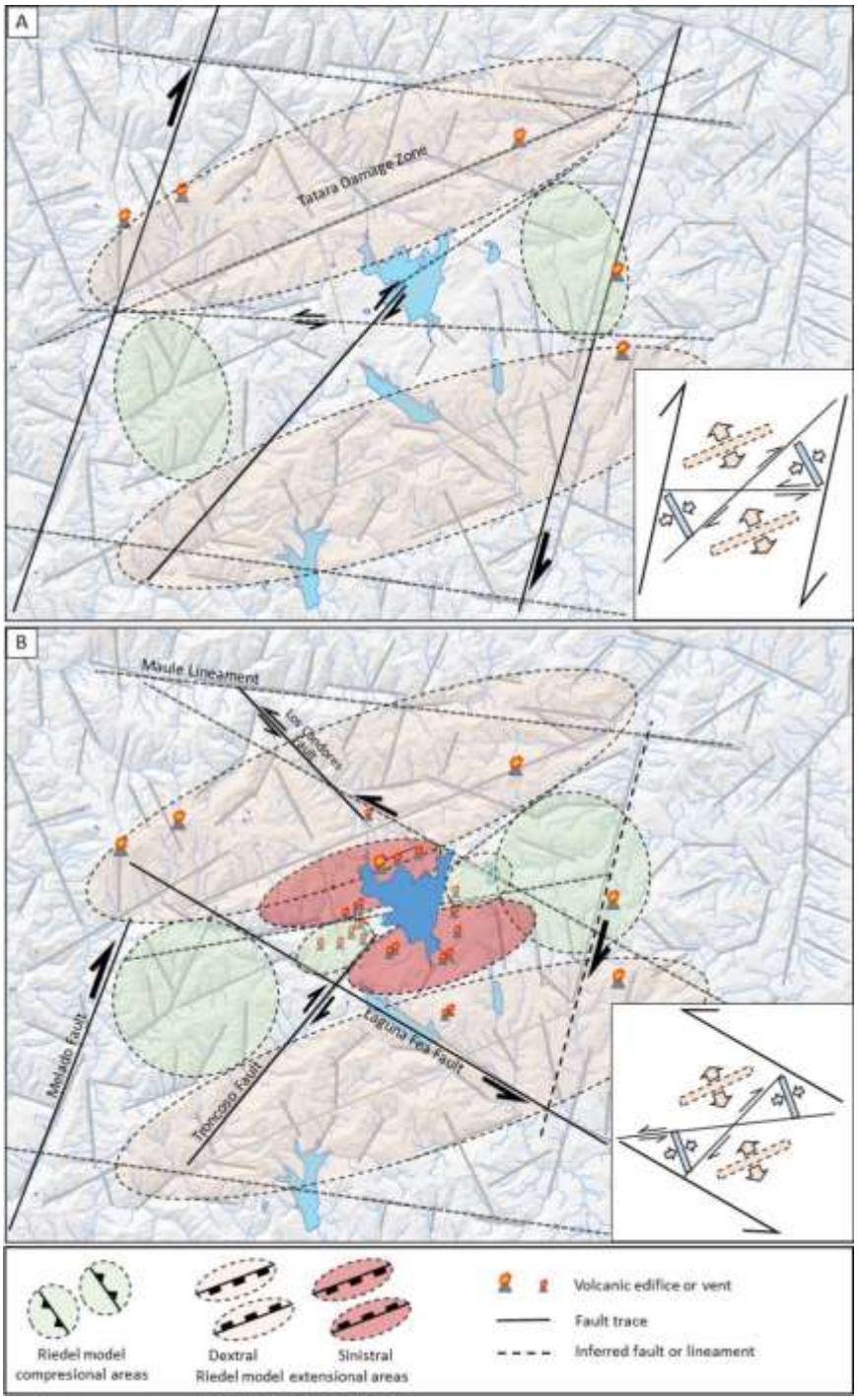

Figure 7. Schematic representation of the tectonic evolution of the Laguna del Maule on the lineament map (grey lines). A) Orogenic scale dextral Riedel system, having the Melado fault as a western master fault. Orange areas represents the theoretical areas in extension, whereas green areas represent areas in compressive regime. The most significative Plio-Pleistocene volcanoes

are also represented. B) Development of an ENE oriented transtensional pull apart basin and having the LdMVC as a depocenter, taking advantage of the Tatara Damage Zone. The reactivation of the NW oriented faults and development of a sinistral Riedel system, favoring the recent volcanism around the Laguna del Maule.

4.2. Drainage pattern as strain marker: advantages and limitations

The geological lineaments acquired via GIS techniques are not consistent even though a variety of manual, semi-automated, and automated techniques are applied (Ahmadi and Pekkan, 2021). Different algorithms recognize, enhance, and extract the linear components of raster images.

Drainage network often reflect the underlying anisotropy of fault damage zones, since they generate local relieve, lithological differences and weaknesses. Moreover, river segments can be classified according to their hierarchical order, and then perform a different treatment for each order. As explained in the methodology, the simplification algorithm derives a representation of the original river network, but in the form of rectilinear segments. In this study, different tolerance thresholds in the line simplification process were assigned to each hierarchical order. The threshold values, selected depending on the valley width, differ between channels of different Strahler order (wider tolerances were used to simplify the segments of higher orders). By applying wide tolerance values for higher order segments, the longest straight segments of main rivers remain preserved. This process also dismisses the local sinuosity due to the dynamics of the river itself or external factors, such as the contribution of sediments from valley sides. Thus, the tolerance threshold used to simplify the river network defines what is accepted as the local sinuosity of a river, without disturbing its linear trend. The tolerance threshold could be

highly variable depending on the geological context and the scale of study, and for this reason, the intrinsic sinuosity and the valley wide of some rivers must be previously verified.

Derive long lineaments from automatic extraction methods is challenging, especially in areas where deformation is dominated by gentle inclined faults following the topography. Their related lineaments become shorter for the more dissected directions, being statistically underestimated. This statistical approach proposed in this study allows to enhance the tectonic signal of the drainage directions, considering that the longest straight segments are probably related to continuous tectonic structures. The method also uses the Strahler hierarchical ordering to give more specific weight to the higher orders segments, without dismiss the information from lower order segments, which tend to have a more isotropic directionality.

In most of geological settings the drainage network undergoes the influences of both factors, geological structures and regional slope (Ribolini and Spagnolo, 2008). At a local scale, relieve can reduce the influence of the bedrock fracture pattern on the arrangement of minor streams (Gioia et al., 2018), whereas at orogenic scale, the drainage network shifts to the almost total influence of the slope when tectonics dismiss (Babault et al., 2012; Saidi et al., 2020). Regions that have uniform environmental conditions and have been largely devoid of tectonic strain, such as passive coastal margins, have predominantly isotropic topography with typically dendritic drainage network patterns (Roy et al., 2016). Then, the relation between drainage and tectonics should not fit very well if drainage pattern is strongly dominated by regional slope.

Regional strain distributes heterogeneously among fault systems but their related lineaments are characterized by periodicity and characteristic spatial pattern also at a local or regional scale (Jordan and Schott, 2005). However, the spatial distribution and population of lineaments in a given orientation can vary significantly according to the observation scale (e.g.

Barth et al., 2012). Therefore, the statistics of lineament orientation also depends on the size of the study area (e.g., Xu et al., 2020). The number, length, and density of lineaments also varies with the spatial resolution of the DEM (e.g., Das and Pardeshi, 2018; Meixner et al., 2018; Rajasekhar et al., 2018; Smith and Wise, 2007; Soliman and Han, 2019). This effect can be observed in this study. For example, the ENE trend do not stand out in the North-Eastern Block (Figure 4), whereas it is the dominant direction in the minor subdomains that cover the southern area of the NEB, but that extend their coverage area to the sides. (Figure 5).

On the other hand, river networks are derived by imposing a variable threshold for the minimum contributing area, which value determines the drainage densities (e.g. Colombo et al., 2007). What is considered a first order channel is relative by definition, since it depends to the minimum contribution area threshold used to derive the drainage network. A given basin can have segments of some hierarchical orders, normally 4-7, depending on the size of the basin. The minimum drainage area considered to be representative should depend on the resolution of the DEM. However, the distribution of azimuth directions for the drainage networks at various threshold levels derives not significantly different results (Radaideh et al., 2016). According to the results of the present study, a minimum contribution area of 0.25 km2 is well adapted to the DEM of 12.5 * 12.5m, assuming that 1600 pixels are enough for the algorithms that calculate flow accumulation and deliver representative values. Any attempt to use a smaller value for minimum catchment area with a low resolution DEM will give inaccurate drainage networks, especially when the drainage network is dense (e.g., Ariza-Villaverde et al., 2015; Ribolini and Spagnolo, 2008). By contrast, the effect of using a higher threshold would be similar to reduce the resolution of the data source (Barth et al., 2012).

In progress studies suggest that this methodology also presents good fit in other areas, but work is being done to better understand the limitations of its application in other morphotectonic contexts. It is also pending for future work to compare the methodology with a better resolution DEM, which would allow to improve the results at a smaller observation scale.

5 Conclusions

This study analyses the drainage pattern to extract lineaments and infer tectonic processes. The spatial distribution of larger lineaments can be used to interpret the tectonic evolution, and aims to better understand the structures involved in the magma rise and volcanism in the LdMVC. The results are consistent with the development of a set of conjugated Riedel systems shearing the Laguna del Maule as a depocenter. An orogenic scale dextral system, having the NNE striking Melado fault as the western master fault, has favored the formation of ENE oriented extensional areas and subsidiary structures. This system is perpendicularly intersected by a local scale sinistral Riedel system, favored by the reactivation of a WNW-NW faults (Laguna Fea and Los Cóndores faults). The orogenic scale dextral Riedel system and the local sinistral Riedel system share the LdMVC as a depocenter, and their subsidiary structures coincides in motion and orientation creating a positive feedback. The extensional areas are oriented ENE, whereas areas in compressional regime trends to NW. Both directions coincide with the path of magma and geofluids broadly described in the SAVZ.

Our results confirm that the analysis of the drainage network directionality is a potential tool for tectonic analysis. The proposed method has been successfully tested in an area with complex tectonic setting, within the intra-arc of the Andes mountain range. Based on remote sensing, it can be particularly useful in predicting the location and orientation of structural

features that would otherwise be impossible to identify and interpret in the field, especially in areas with difficult access, covered by dense vegetation, or with discontinuous outcrops.

Acknowledgments

This research was supported by the Dirección de Investigación of the Universidad Católica de Temuco (project 2020EM-AP-12). Author is thankful to Miquel Pastor and Dr. Isaac Corral for early discussions. Author thankfully acknowledge Gerd Sielfeld, Nico Garibaldi and coauthors for provide field measurements and contributions in the study area.

The author declares that he has no known competing financial interests or personal relationships that could have appeared to influence the work reported in this paper.

References

Abdullah, A., Akhir, J. M., & Abdullah, I. (2010). Automatic mapping of lineaments using shaded relief images derived from digital elevation model (DEMs) in the Maran–Sungi Lembing area, Malaysia. Electronic Journal of Geotechnical Engineering, 15(6), 949–958.

Acocella, V., Funiciello, R., Marotta, E., Orsi, G., & de Vita, S. (2004). The role of extensional structures on experimental calderas and resurgence. Journal of Volcanology and Geothermal Research, 129, 199–217. https://doi.org/10.1016/S0377-0273(03)00240-3

Adiri, Z., El Harti, A., Jellouli, A., Lhissou, R., Maacha, L., Azmi, M., et al. (2017). Comparison of Landsat-8, ASTER and Sentinel 1 satellite remote sensing data in automatic lineaments extraction: A case study of Sidi Flah-Bouskour inlier, Moroccan Anti Atlas. Advances in Space Research, 60(11), 2355–2367.

Ahmadi, H., & Pekkan, E. (2021). Fault-Based Geological Lineaments Extraction Using Remote Sensing and GIS—A Review. Geosciences . https://doi.org/10.3390/geosciences11050183

587 Andersen, N. L., Singer, B. S., Jicha, B. R., Beard, B. L., Johnson, C. M., & Licciardi, J. M. (2017). Pleistocene to
588 Holocene Growth of a Large Upper Crustal Rhyolitic Magma Reservoir beneath the Active Laguna del Maule
589 Volcanic Field, Central Chile. Journal of Petrology, 58(1), 85–114. https://doi.org/10.1093/petrology/egx006

590 Ariza-Villaverde, A. B., Jiménez-Hornero, F. J., & Gutiérrez de Ravé, E. (2015). Influence of DEM resolution on
591 drainage network extraction: A multifractal analysis. Geomorphology, 241, 243–254.
592 https://doi.org/https://doi.org/10.1016/j.geomorph.2015.03.040

593 Babault, J., Van Den Driessche, J., & Teixell, A. (2012). Longitudinal to transverse drainage network evolution in
594 the High Atlas (Morocco): The role of tectonics. Tectonics, 31(4).

595 Barth, N. C., Toy, V. G., Langridge, R. M., & Norris, R. J. (2012). Scale dependence of oblique plate-boundary
596 partitioning: New insights from LiDAR, central Alpine fault, New Zealand. Lithosphere, 4(5), 435–448.

597 Beneduce, P., Festa, V., Francioso, R., Schiattarella, M., & Tropeano, M. (2004). Conflicting drainage patterns in
598 the Matera Horst Area, southern Italy. Physics and Chemistry of the Earth, Parts A/B/C, 29(10), 717–724.

599 Bishop, P., Hoey, T. B., Jansen, J. D., & Artza, I. L. (2005). Knickpoint recession rate and catchment area: the case
600 of uplifted rivers in Eastern Scotland. Earth Surface Processes and Landforms, 30(6), 767–778.
601 https://doi.org/10.1002/esp.1191

602 Brocard, G., Teyssier, C., Dunlap, W. J., Authemayou, C., Simon-Labric, T., Cacao-Chiquín, E. N., et al. (2011).
603 Reorganization of a deeply incised drainage: role of deformation, sedimentation and groundwater flow. Basin
604 Research, 23(6), 631–651. https://doi.org/10.1111/j.1365-2117.2011.00510.x

605 Cardona, C., Tassara, A., Gil-Cruz, F., Lara, L., Morales, S., Kohler, P., & Franco, L. (2018). Crustal seismicity
606 associated to rpid surface uplift at Laguna del Maule Volcanic Complex, Southern Volcanic Zone of the Andes.
607 Journal of Volcanology and Geothermal Research, 353, 83–94.
608 https://doi.org/10.1016/J.JVOLGEORES.2018.01.009

609 Castelltort, S., Goren, L., Willett, S. D., Champagnac, J.-D., Herman, F., & Braun, J. (2012). River drainage patterns
610 in the New Zealand Alps primarily controlled by plate tectonic strain. Nature Geoscience, 5(10), 744–748.
611 https://doi.org/10.1038/ngeo1582

612 Cembrano, J., & Lara, L. (2009). The link between volcanism and tectonics in the southern volcanic zone of the
613 Chilean Andes: A review. Tectonophysics, 471(1), 96–113.
614 https://doi.org/https://doi.org/10.1016/j.tecto.2009.02.038

615 Colombo, R., Vogt, J. V, Soille, P., Paracchini, M. L., & de Jager, A. (2007). Deriving river networks and
616 catchments at the European scale from medium resolution digital elevation data. CATENA, 70(3), 296–305.
617 https://doi.org/https://doi.org/10.1016/j.catena.2006.10.001

618 Das, S., & Pardeshi, S. D. (2018). Comparative analysis of lineaments extracted from Cartosat, SRTM and ASTER
619 DEM: a study based on four watersheds in Konkan region, India. Spatial Information Research, 26(1), 47–57.

620 Douglas, D. H., & Peucker, T. K. (1973). Algorithms for the reduction of the number of points required to represent
621 a digitized line or its caricature. Cartographica: The International Journal for Geographic Information and
622 Geovisualization, 10(2), 112–122.

623 Duvall, A. R., Harbert, S. A., Upton, P., Tucker, G. E., Flowers, R. M., & Collett, C. (2020). River patterns reveal
624 two stages of landscape evolution at an oblique convergent margin, Marlborough Fault System, New Zealand. Earth
625 Surf. Dynam., 8(1), 177–194. https://doi.org/10.5194/esurf-8-177-2020

626 Farahbakhsh, E., Chandra, R., Olierook, H. K. H., Scalzo, R., Clark, C., Reddy, S. M., & Müller, R. D. (2020).
627 Computer vision-based framework for extracting tectonic lineaments from optical remote sensing data. International
628 Journal of Remote Sensing, 41(5), 1760–1787.

629 Feigl, K. L., Le Mével, H., Tabrez Ali, S., Córdova, L., Andersen, N. L., DeMets, C., & Singer, B. S. (2014). Rapid
630 uplift in Laguna del Maule volcanic field of the Andean Southern Volcanic zone (Chile) 2007–2012. Geophysical
631 Journal International, 196(2), 885–901.

632 Flores-Prieto, E., Quénéhervé, G., Bachofer, F., Shahzad, F., & Maerker, M. (2015). Morphotectonic interpretation
633 of the Makuyuni catchment in Northern Tanzania using DEM and SAR data. Geomorphology, 248, 427–439.

634 Fournier, T. J., Pritchard, M. E., & Riddick, S. N. (2010). Duration, magnitude, and frequency of subaerial volcano
635 deformation events: New results from Latin America using InSAR and a global synthesis. Geochemistry,
636 Geophysics, Geosystems, 11(1).

637 Garibaldi, N., Tikoff, B., Peterson, D., Davis, J. R., & Keranen, K. (2020). Statistical separation of tectonic and
638 inflation-driven components of deformation on silicic reservoirs, Laguna del Maule volcanic field, Chile. Journal of
639 Volcanology and Geothermal Research, 389, 106744.

640 Giambiagi, L., Álvarez, P., Spagnotto, S., Godoy, E., Lossada, A., Mescua, J., et al. (2019). Geomechanical model
641 for a seismically active geothermal field: Insights from the Tinguiririca volcanic-hydrothermal system. Geoscience
642 Frontiers, 10(6), 2117–2133. https://doi.org/https://doi.org/10.1016/j.gsf.2019.02.006

643 Gioia, D., Schiattarella, M., & Giano, S. I. (2018). Right-angle pattern of minor fluvial networks from the Ionian
644 terraced belt, southern Italy: passive structural control or foreland bending? Geosciences, 8(9), 331.

645 Grohmann, C. H. (2004). Morphometric analysis in geographic information systems: applications of free software
646 GRASS and R. Computers & Geosciences, 30(9–10), 1055–1067.

647 Guerit, L., Dominguez, S., Malavieille, J., & Castelltort, S. (2016). Deformation of an experimental drainage
648 network in oblique collision. Tectonophysics, 693, 210–222.
649 https://doi.org/https://doi.org/10.1016/j.tecto.2016.04.016

650 Hallet, B., & Molnar, P. (2001). Distorted drainage basins as markers of crustal strain east of the Himalaya. Journal
651 of Geophysical Research: Solid Earth, 106(B7), 13697–13709.
652 https://doi.org/https://doi.org/10.1029/2000JB900335

653 Han, L., Liu, Z., Ning, Y., & Zhao, Z. (2018). Extraction and analysis of geological lineaments combining a DEM
654 and remote sensing images from the northern Baoji loess area. Advances in Space Research, 62(9), 2480–2493.

655 Hashim, M., Ahmad, S., Johari, M. A. M., & Pour, A. B. (2013). Automatic lineament extraction in a heavily
656 vegetated region using Landsat Enhanced Thematic Mapper (ETM+) imagery. Advances in Space Research, 51(5),
657 874–890.

658 Hildreth, W. (2010). Laguna del Maule Volcanic Field: Eruptive History of a Quaternary basalt-to-rhyolite
659 distributed volcanic field on the Andean rangecrest in central Chile. Servicio Nacional de Geología y Minería-Chile.

660 Hodgkinson, J. H., McLoughlin, S., & Cox, M. (2006). The influence of geological fabric and scale on drainage
661 pattern analysis in a catchment of metamorphic terrain: Laceys Creek, southeast Queensland, Australia.
662 Geomorphology, 81(3–4), 394–407.

Hung, L. Q., Batelaan, O., & Smedt, F. De. (2005). Lineament extraction and analysis, comparison of LANDSAT ETM and ASTER imagery. Case study: Suoimuoi tropical karst catchment, Vietnam. In Proc.SPIE (Vol. 5983). Retrieved from https://doi.org/10.1117/12.627699

Jenson, S. K., & Domingue, J. O. (1988). Extracting topographic structure from digital elevation data for geographic information system analysis. Photogrammetric Engineering and Remote Sensing, 54(11), 1593–1600.

Jordan, G., & Schott, B. (2005). Application of wavelet analysis to the study of spatial pattern of morphotectonic lineaments in digital terrain models. A case study. Remote Sensing of Environment, 94(1), 31–38. https://doi.org/https://doi.org/10.1016/j.rse.2004.08.013

Jordán, G., Meijninger, B. M. L., Van Hinsbergen, D. J. J., Meulenkamp, J. E., & Van Dijk, P. M. (2005). Extraction of morphotectonic features from DEMs: Development and applications for study areas in Hungary and NW Greece. International Journal of Applied Earth Observation and Geoinformation, 7(3), 163–182.

Keller, E. A., & Pinter, N. (1996). Active tectonics (Vol. 338). Prentice Hall Upper Saddle River, NJ.

Koike, K., Nagano, S., & Kawaba, K. (1998). Construction and analysis of interpreted fracture planes through combination of satellite-image derived lineaments and digital elevation model data. Computers & Geosciences, 24(6), 573–583.

Lavenu, A., & Cembrano, J. (1999). Compressional- and transpressional-stress pattern for Pliocene and Quaternary brittle deformation in fore arc and intra-arc zones (Andes of Central and Southern Chile). Journal of Structural Geology, 21(12), 1669–1691. https://doi.org/https://doi.org/10.1016/S0191-8141(99)00111-X

Levy, S., Bohnenstiehl, D. R., Sprinkle, P., Boettcher, M. S., Wilcock, W. S. D., Tolstoy, M., & Waldhauser, F. (2018). Mechanics of fault reactivation before, during, and after the 2015 eruption of Axial Seamount. Geology, 46(5), 447–450.

Liu, R., Miao, Q., Song, J., Quan, Y., Li, Y., Xu, P., & Dai, J. (2019). Multiscale road centerlines extraction from high-resolution aerial imagery. Neurocomputing, 329, 384–396.

Magee, C., O'DRISCOLL, B., & Chambers, A. D. (2010). Crystallization and textural evolution of a closed-system magma chamber: insights from a crystal size distribution study of the Lilloise layered intrusion, East Greenland. Geological Magazine, 147(3), 363–379.

689 Marghany, M., & Hashim, M. (2010). Lineament mapping using multispectral remote sensing satellite data.
690 International Journal of Physical Sciences, 5(10), 1501–1507.

691 Masoud, A., & Koike, K. (2017). Applicability of computer-aided comprehensive tool (LINDA: LINeament
692 Detection and Analysis) and shaded digital elevation model for characterizing and interpreting morphotectonic
693 features from lineaments. Computers & Geosciences, 106, 89–100.

694 Meixner, J., Grimmer, J. C., Becker, A., Schill, E., & Kohl, T. (2018). Comparison of different digital elevation
695 models and satellite imagery for lineament analysis: Implications for identification and spatial arrangement of fault
696 zones in crystalline basement rocks of the southern Black Forest (Germany). Journal of Structural Geology, 108,
697 256–268.

698 Le Mével, H., Feigl, K. L., Córdova, L., DeMets, C., & Lundgren, P. (2015). Evolution of unrest at Laguna del
699 Maule volcanic field (Chile) from InSAR and GPS measurements, 2003 to 2014. Geophysical Research Letters,
700 42(16), 6590–6598.

701 Le Mével, H., Gregg, P. M., & Feigl, K. L. (2016). Magma injection into a long-lived reservoir to explain
702 geodetically measured uplift: Application to the 2007–2014 unrest episode at Laguna del Maule volcanic field,
703 Chile. Journal of Geophysical Research: Solid Earth, 121(8), 6092–6108. https://doi.org/10.1002/2016JB013066

704 Miller, C. A., Williams-Jones, G., Fournier, D., & Witter, J. (2017). 3D gravity inversion and thermodynamic
705 modelling reveal properties of shallow silicic magma reservoir beneath Laguna del Maule, Chile. Earth and
706 Planetary Science Letters, 459, 14–27. https://doi.org/10.1016/J.EPSL.2016.11.007

707 Molnar, P., Anderson, R. S., & Anderson, S. P. (2007). Tectonics, fracturing of rock, and erosion. Journal of
708 Geophysical Research: Earth Surface, 112(F3). https://doi.org/https://doi.org/10.1029/2005JF000433

709 Narciso, V., Santamaria, G., & Zanettini, J. C. (2004). Hoja Geológica 3769-I Barrancas Provincias de Mendoza y
710 Neuquén. Boletín Del Instituto de Geología y Recursos Minerales, Servicio Geológico Minero Argentino.

711 Pardo-Casas, F., & Molnar, P. (1987). Relative motion of the Nazca (Farallon) and South American Plates since
712 Late Cretaceous time. Tectonics, 6(3), 233–248. https://doi.org/https://doi.org/10.1029/TC006i003p00233

713 Pastor, A., Babault, J., Teixell, A., & Arboleya, M. L. (2012). Intrinsic stream-capture control of stepped fan
714 pediments in the High Atlas piedmont of Ouarzazate (Morocco). Geomorphology, 173–174, 88–103.
715 https://doi.org/https://doi.org/10.1016/j.geomorph.2012.05.032

716 Pearce, R. K., Sánchez de la Muela, A., Moorkamp, M., Hammond, J. O. S., Mitchell, T. M., Cembrano, J., et al.
717 (2020). Reactivation of Fault Systems by Compartmentalized Hydrothermal Fluids in the Southern Andes Revealed
718 by Magnetotelluric and Seismic Data. Tectonics, 39(12), e2019TC005997.
719 https://doi.org/https://doi.org/10.1029/2019TC005997

720 Pérez-Flores, P., Cembrano, J., Sánchez-Alfaro, P., Veloso, E., Arancibia, G., & Roquer, T. (2016). Tectonics,
721 magmatism and paleo-fluid distribution in a strike-slip setting: Insights from the northern termination of the
722 Liquiñe–Ofqui fault System, Chile. Tectonophysics, 680, 192–210.

723 Perron, J. T., Richardson, P. W., Ferrier, K. L., & Lapôtre, M. (2012). The root of branching river networks. Nature,
724 492(7427), 100–103. https://doi.org/10.1038/nature11672

725 Peterson, D. E., Garibaldi, N., Keranen, K., Tikoff, B., Miller, C., Lara, L. E., et al. (2020). Active Normal Faulting,
726 Diking, and Doming Above the Rapidly Inflating Laguna del Maule Volcanic Field, Chile, Imaged With CHIRP,
727 Magnetic, and Focal Mechanism Data. Journal of Geophysical Research: Solid Earth, 125(8), e2019JB019329.

728 Radaideh, O. M. A., Grasemann, B., Melichar, R., & Mosar, J. (2016). Detection and analysis of morphotectonic
729 features utilizing satellite remote sensing and GIS: An example in SW Jordan. Geomorphology, 275, 58–79.
730 https://doi.org/https://doi.org/10.1016/j.geomorph.2016.09.033

731 Rajasekhar, M., Raju, G. S., Raju, R. S., Ramachandra, M., & Kumar, B. P. (2018). Data on comparative studies of
732 lineaments extraction from ASTER DEM, SRTM, and Cartosat for Jilledubanderu River basin, Anantapur district,
733 A.P, India by using remote sensing and GIS. Data in Brief, 20, 1676–1682.
734 https://doi.org/https://doi.org/10.1016/j.dib.2018.09.023

735 Ramsay, J. G., & Huber, M. I. (1987). The techniques of modern structural geology: Folds and fractures (Vol. 2).
736 Academic press.

737 Resmi, M. R., Babeesh, C., & Achyuthan, H. (2019). Quantitative analysis of the drainage and morphometric
738 characteristics of the Palar River basin, Southern Peninsular India; using bAd calculator (bearing azimuth and

739 drainage) and GIS. Geology, Ecology, and Landscapes, 3(4).
740 https://doi.org/http://dx.doi.org/10.1080/24749508.2018.1563750

741 Reyes-Wagner, V., Díaz, D., Cordell, D., & Unsworth, M. (2017). Regional electrical structure of the Andean
742 subduction zone in central Chile (35°–36°S) using magnetotellurics. Earth, Planets and Space, 69(1), 142.
743 https://doi.org/10.1186/s40623-017-0726-z

744 Ribolini, A., & Spagnolo, M. (2008). Drainage network geometry versus tectonics in the Argentera Massif (French–
745 Italian Alps). Geomorphology, 93(3–4), 253–266.

746 Rosenau, M., Melnick, D., & Echtler, H. (2006). Kinematic constraints on intra-arc shear and strain partitioning in
747 the southern Andes between 38°S and 42°S latitude. Tectonics, 25(4).
748 https://doi.org/https://doi.org/10.1029/2005TC001943

749 Roy, S. G., Koons, P. O., Upton, P., & Tucker, G. E. (2016). Dynamic links among rock damage, erosion, and strain
750 during orogenesis. Geology, 44(7), 583–586. https://doi.org/10.1130/G37753.1

751 Ruz, J., Browning, J., Cembrano, J., Iturrieta, P., Gerbault, M., & Sielfeld, G. (2020). Field observations and
752 numerical models of a Pleistocene-Holocene feeder dyke swarm associated with a fissure complex to the east of the
753 Tatara-San Pedro-Pellado complex, Southern Volcanic Zone, Chile. Journal of Volcanology and Geothermal
754 Research, 404, 107033. https://doi.org/https://doi.org/10.1016/j.jvolgeores.2020.107033

755 Saidi, A., Bouramtane, T., Achab, M., Kassou, N., Kacimi, I., Tahiri, A., & Valles, V. (2020). The Hough transform
756 algorithm coupled with spatial filtering for the study of geological structuring control on the drainage network:
757 application to the North Oulmes region, Morocco. Arabian Journal of Geosciences, 13(19), 1–17.

758 Shahzad, F., Mahmood, S. A., & Gloaguen, R. (2009). Drainage network and lineament analysis: An approach for
759 Potwar Plateau (Northern Pakistan). Journal of Mountain Science, 6(1), 14. https://doi.org/10.1007/s11629-009-
760 0206-4

761 Sielfeld, G., Lange, D., & Cembrano, J. (2019). Intra-Arc Crustal Seismicity: Seismotectonic Implications for the
762 Southern Andes Volcanic Zone, Chile. Tectonics, 38(2), 552–578.
763 https://doi.org/https://doi.org/10.1029/2018TC004985

764 Sielfeld, G., Ruz, J., Brogi, A., Cembrano, J., Stanton-Yonge, A., Pérez-Flores, P., & Iturrieta, P. (2019). Oblique-
765 slip tectonics in an active volcanic chain: A case study from the Southern Andes. Tectonophysics, 770, 228221.
766 https://doi.org/10.1016/J.TECTO.2019.228221

767 Singer, B S, Thompson, R. A., Dungan, M. A., Feeley, T. C., Nelson, S. T., Pickens, J. C., et al. (1997). Volcanism
768 and erosion during the past 930 ky at the Tatara–San Pedro complex, Chilean Andes. Geological Society of America
769 Bulletin, 109(2), 127–142.

770 Singer, Brad S, Andersen, N. L., Le Mével, H., Feigl, K. L., DeMets, C., Tikoff, B., et al. (2014). Dynamics of a
771 large, restless, rhyolitic magma system at Laguna del Maule, southern Andes, Chile. GSA Today, 24(12), 4–10.

772 Singer, Brad S, Le Mével, H., Licciardi, J. M., Córdova, L., Tikoff, B., Garibaldi, N., et al. (2018). Geomorphic
773 expression of rapid Holocene silicic magma reservoir growth beneath Laguna del Maule, Chile. Science Advances,
774 4(6), eaat1513. https://doi.org/10.1126/sciadv.aat1513

775 Smith, M. J., & Wise, S. M. (2007). Problems of bias in mapping linear landforms from satellite imagery.
776 International Journal of Applied Earth Observation and Geoinformation, 9(1), 65–78.

777 Soliman, A., & Han, L. (2019). Effects of vertical accuracy of digital elevation model (DEM) data on automatic
778 lineaments extraction from shaded DEM. Advances in Space Research, 64(3), 603–622.

779 Solomon, S., & Ghebreab, W. (2006). Lineament characterization and their tectonic significance using Landsat TM
780 data and field studies in the central highlands of Eritrea. Journal of African Earth Sciences, 46(4), 371–378.

781 Soto-Pinto, C., Arellano-Baeza, A., & Sánchez, G. (2013). A new code for automatic detection and analysis of the
782 lineament patterns for geophysical and geological purposes (ADALGEO). Computers & Geosciences, 57, 93–103.

783 Stanton-Yonge, A., Griffith, W. A., Cembrano, J., St. Julien, R., & Iturrieta, P. (2016). Tectonic role of margin-
784 parallel and margin-transverse faults during oblique subduction in the Southern Volcanic Zone of the Andes:
785 Insights from Boundary Element Modeling. Tectonics, 35(9), 1990–2013.
786 https://doi.org/https://doi.org/10.1002/2016TC004226

787 Strahler, A. N. (1964). Quantitative geomorphology of drainage basin and channel networks. Handbook of Applied
788 Hydrology.

Suzen, M. L., & Toprak, V. (1998). Filtering of satellite images in geological lineament analyses: an application to a fault zone in Central Turkey. International Journal of Remote Sensing, 19(6), 1101–1114.

Tarboton, D. G., Bras, R. L., & Rodriguez-Iturbe, I. (1991). On the extraction of channel networks from digital elevation data. Hydrological Processes, 5(1), 81–100.

Tripathi, N. K., Gokhale, K., & Siddiqui, M. U. (2000). Directional morphological image transforms for lineament extraction from remotely sensed images. International Journal of Remote Sensing, 21(17), 3281–3292.

Wu, J. E., McClay, K., Whitehouse, P., & Dooley, T. (2009). 4D analogue modelling of transtensional pull-apart basins. Marine and Petroleum Geology, 26(8), 1608–1623. https://doi.org/https://doi.org/10.1016/j.marpetgeo.2008.06.007

Xu, J., Wen, X., Zhang, H., Luo, D., Li, J., Xu, L., & Yu, M. (2020). Automatic extraction of lineaments based on wavelet edge detection and aided tracking by hillshade. Advances in Space Research, 65(1), 506–517.

Yun, S.-H., & Moon, W. (2001). Lineament extraction from DEM using drainage network. International Geoscience and Remote Sensing Symposium (IGARSS) (Vol. 5). https://doi.org/10.1109/IGARSS.2001.977994